Semi Annual Report
of the work of
The Bartol Research Foundation of
The Franklin Institute
Performed under Contract Nonr436(00
February 1, 1953--June 30, 1953

SEMI ANNUAL REPORT

of the Work of the

BARTOL RESEARCH FOUNDATION

OF THE FRANKLIN INSTITUTE

(February 1, 1953 -- June 30, 1953)

Performed Under Contract Nonr 436(00)

with the

OFFICE OF NAVAL RESEARCH

TABIE OF CONTENTS

TABLE OF CONTENTS

## PERSONNEL

**Physicists:** (Part-time or full-time)

D. W. Kent

C. E. Mandeville

F. R. Metzger

M. A. Rothman

S. C. Snowdon

W. D. Whitehead

**Technicians:** (Half-time)

R. W. Gunnett

Report submitted July 30, 1953

C. E. Mandeville

C. E. Mandeville, Physicist

# I. INELASTIC SCATTERING.

## MEASUREMENT OF NEUTRON ENERGIES

In the foregoing semi-annual report, results were presented concerning neutron scattering from iron. A survey of various geometries was carried out with the idea of obtaining one which provided good resolution and at the same time was relatively simple. One of the geometries which appeared promising was that of the 20-cm "paraffin wedge". This arrangement is depicted in Figure 1. As a trial scatterer, a cylinder of chromium was employed. The scattered neutrons were detected at an angle of $90^{\circ}$ with the incident neutrons. A background run was taken with no scatterer present. The accumulated background was subtracted from the data obtained when the scatterer was present. The background data as well as those with scatterer present were normalized to take properly into account the incident neutron flux and the plate-area scanned. The resulting spectrum is shown in Figure 2 where it is clear that three resolved groups of neutrons are present. The group of greatest energy is the elastically scattered one. The two groups of neutrons at lower energies result from the inelastic scattering process. They would correspond to formation of $Cr^{52}$ in excited states at $\sim$1.43 and $\sim$1.93 Mev. The broken line is the energy distribution of recoil protons corrected for variation with energy of the n-p scattering cross section and acceptance probability.

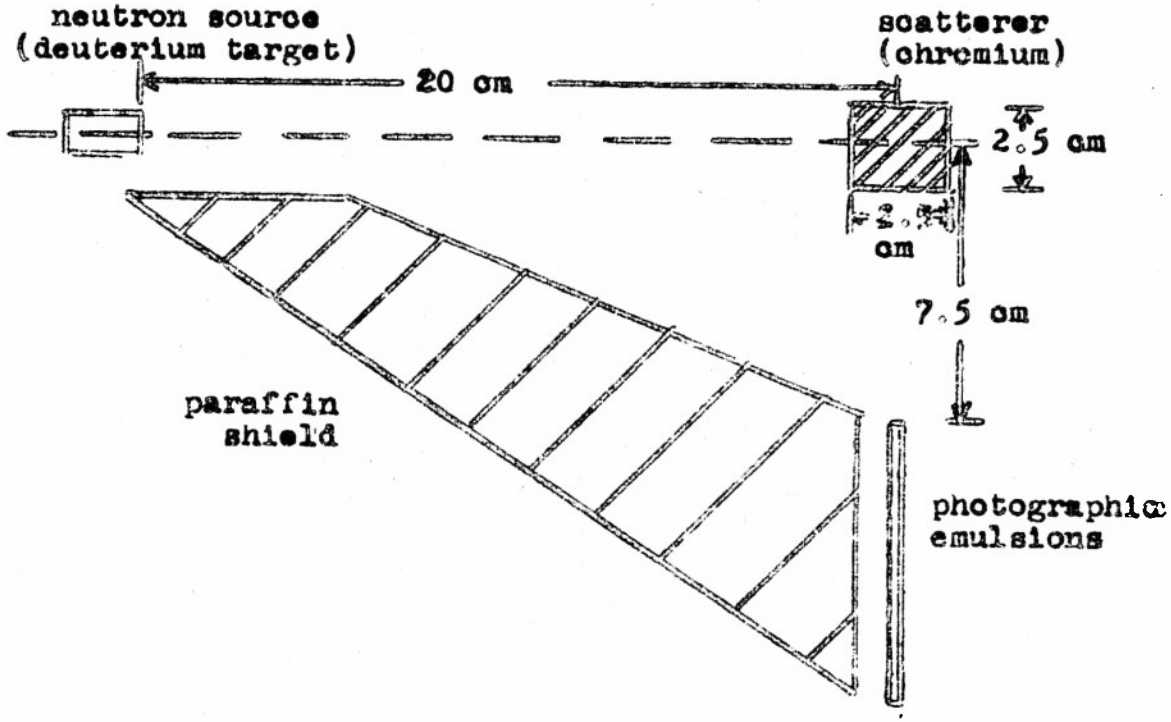


GEOMETRY FOR DETECTION OF NEUTRONS SCATTERED FROM CHROMIUM

Figure 1

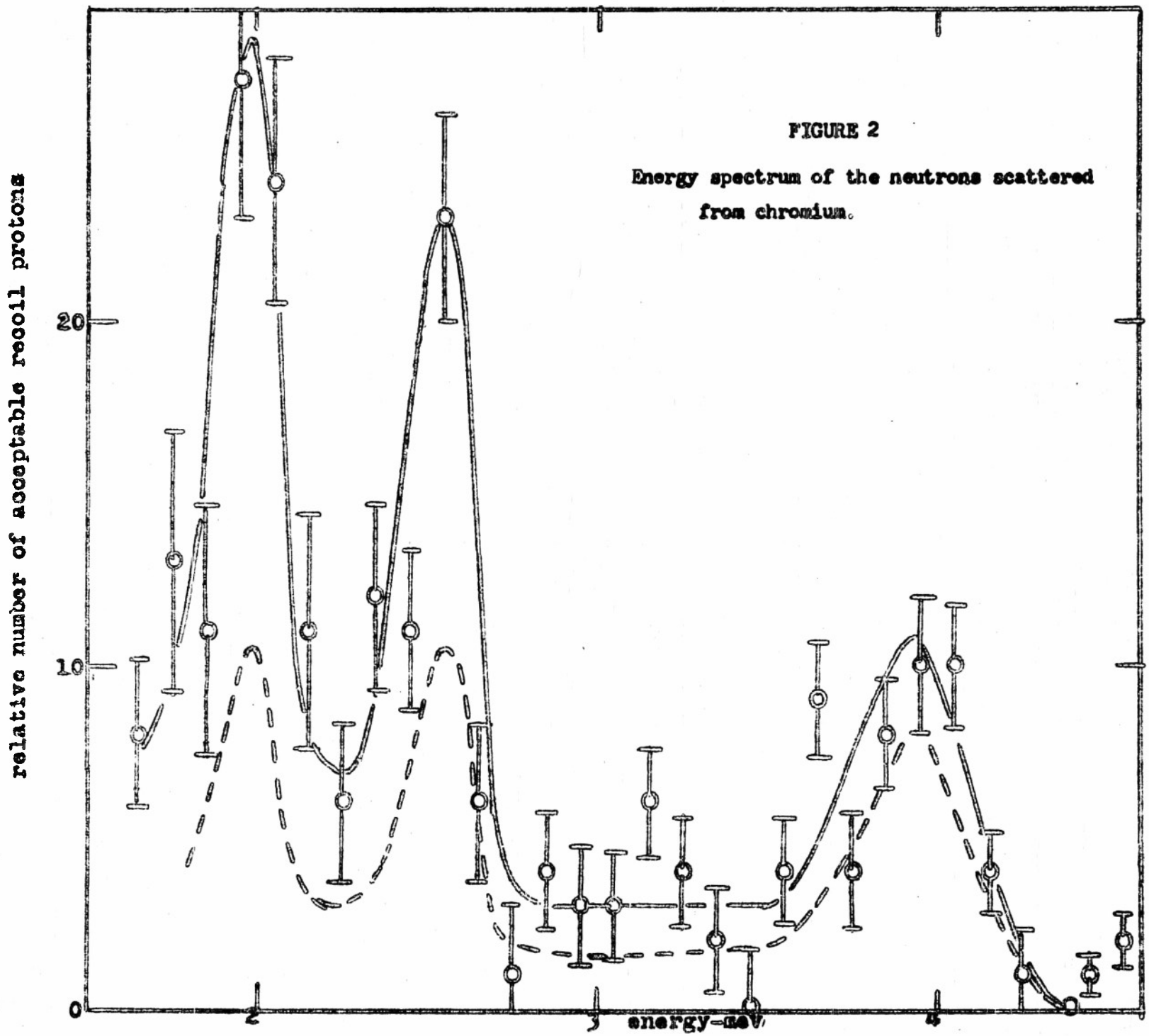


FIGURE 2

Energy spectrum of the neutrons scattered from chromium.

The gamma rays from neutron scattering in chromium and their relation to the neutron spectrum will be discussed in a later section of this report.

## GAMMA-RAY MEASUREMENTS

A geometry for detecting gamma rays excited in the inelastic scattering process is given in Figure 3. In this arrangement, neutrons are produced in the D-D reaction at the target of the Van de Graaff statitron and proceed to the scattering ring of material about the crystal of NaI-Tl. There they are detected, and the pulse-height distribution is observed in a single channel pulse-height discriminator.

The procedure adopted was to measure the background in the scintillation detector and then measure the total counting rate, background and contribution from the scatterer included. The background was measured in each interval of two volts, the dummy scatterer being a graphite ring. Since the first excited level of $C^{12}$ is at 4.43 Mev, the carbon ring contributed no gamma ray arising from any inelastic scattering effects. It was not considered correct to take the measured counting rate with no scatterer present at all as the background, because the scattering ring deflects neutrons into the crystal giving rise to capture gamma rays and to radioactivity, the 25-minute iodine. The high energy beta-ray spectrum of this radioisotope contributes materially to the background count.

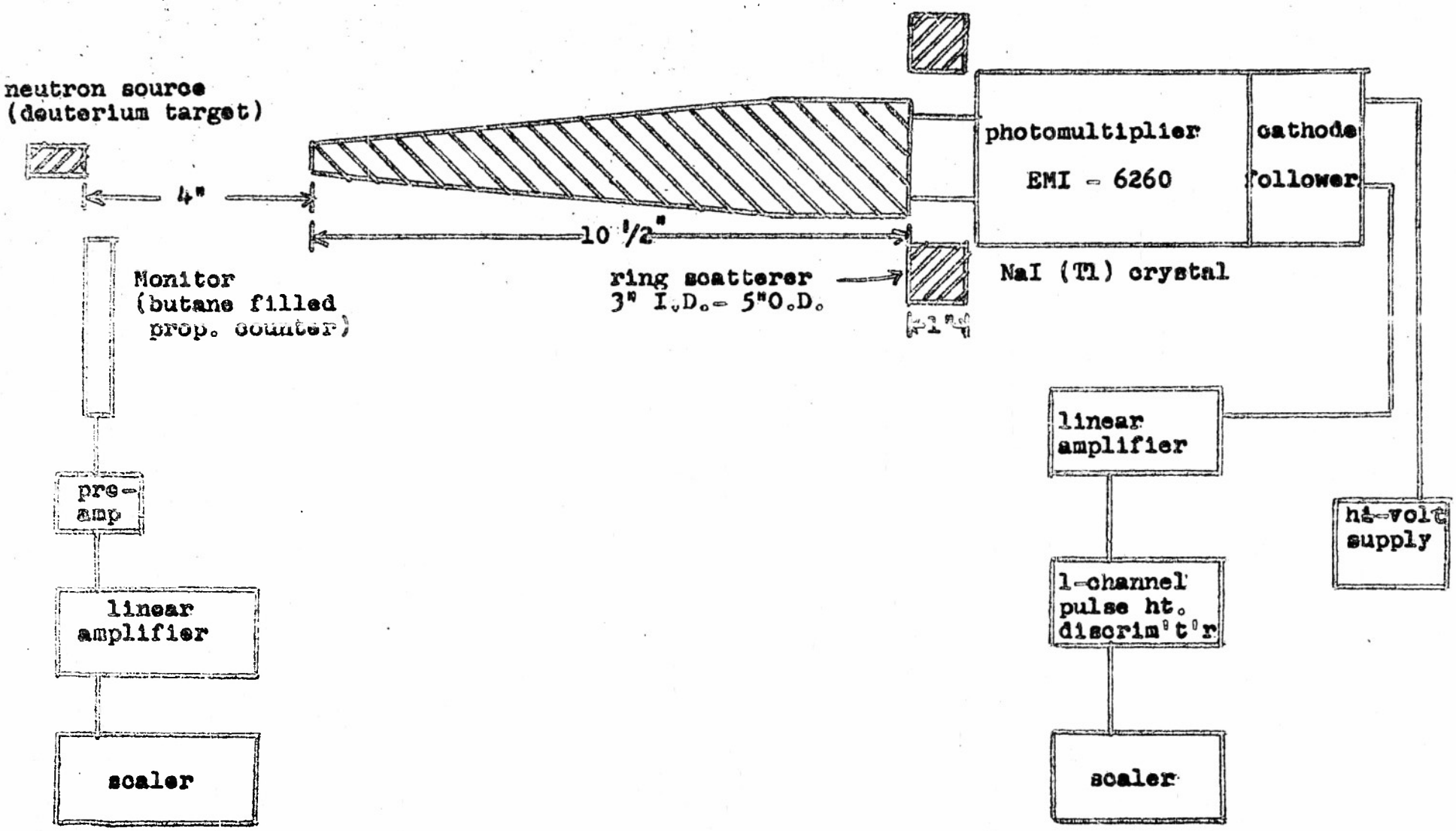


GEOMETRY AND CIRCUITRY OF SCINTILLATION COUNTING EXPERIMENT

FIGURE 3

In Figure 4 is the pulse-height distribution of the gamma rays resulting from the scattering of 3.9 Mev gamma rays by chromium along with the background obtained with the carbon ring replacing the metallic scatterer. It should perhaps be remarked that no measurements of any kind were commenced until after the Van de Graaff had been producing neutrons for more than an hour to bring to approximate equilibrium the 25-minute activity. In Figure 5, similar curves are presented for graphite and lead.

In Figures 6, 7, 8, and 9 are pulse-height distributions with background subtracted of gamma rays emitted in the inelastic scattering process by iron, bismuth, chromium, and lead. The energies and relative intensities of the gamma rays are summarized in Table I.

TABLE I.

| Element | Gamma Rays (Energies, Mev) | Relative Intensities |
|---|---|---|
| iron | 0.85<br>2.15 | 680<br>260 |
| bismuth | 0.90<br>1.63<br>2.66 | 540<br>1000<br>600 |
| lead | 0.84<br>1.55<br>2.66 | 400<br>650<br>450 |
| chromium | 1.43 | - - - |

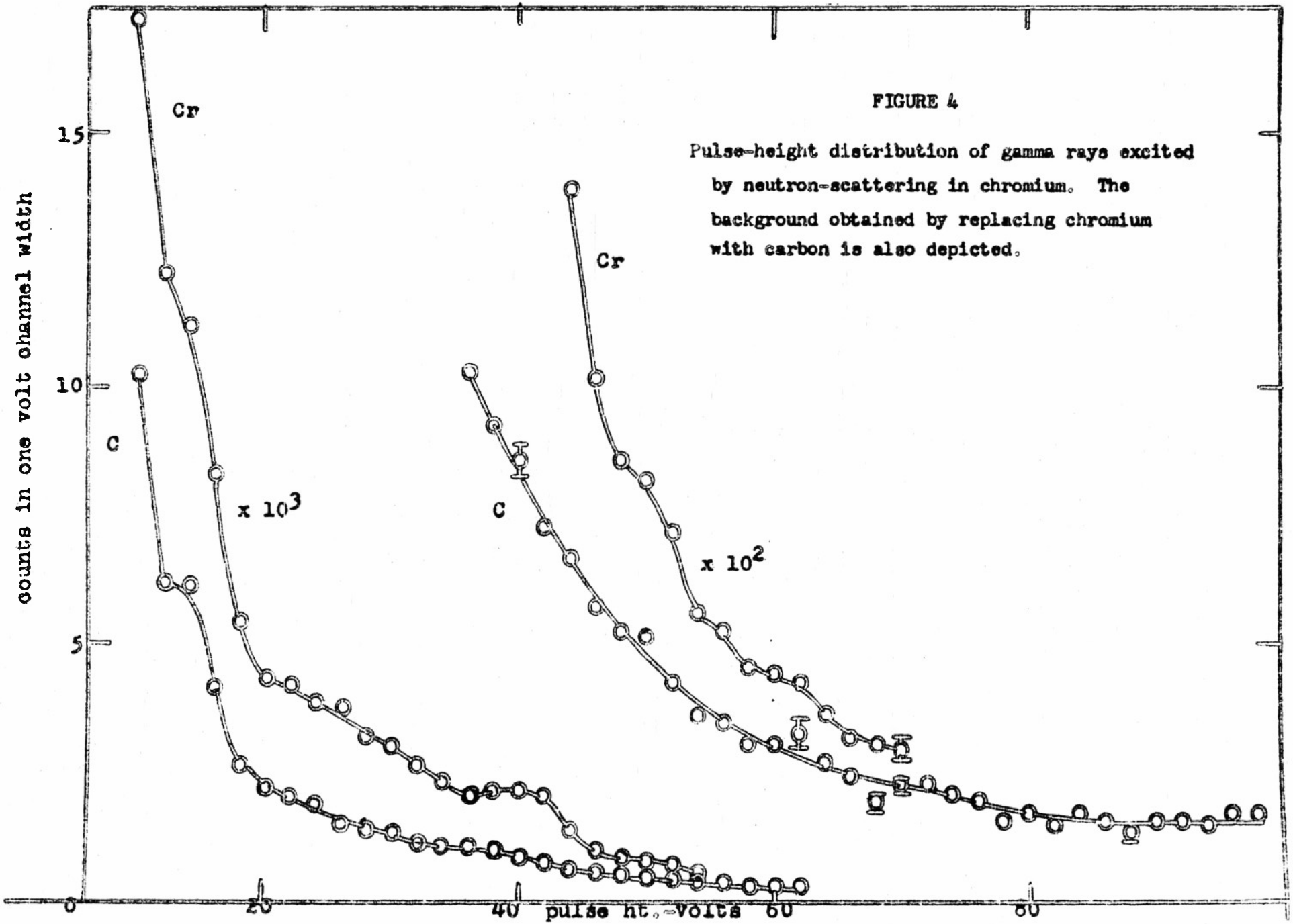


FIGURE 4

Pulse-height distribution of gamma rays excited by neutron-scattering in chromium. The background obtained by replacing chromium with carbon is also depicted.

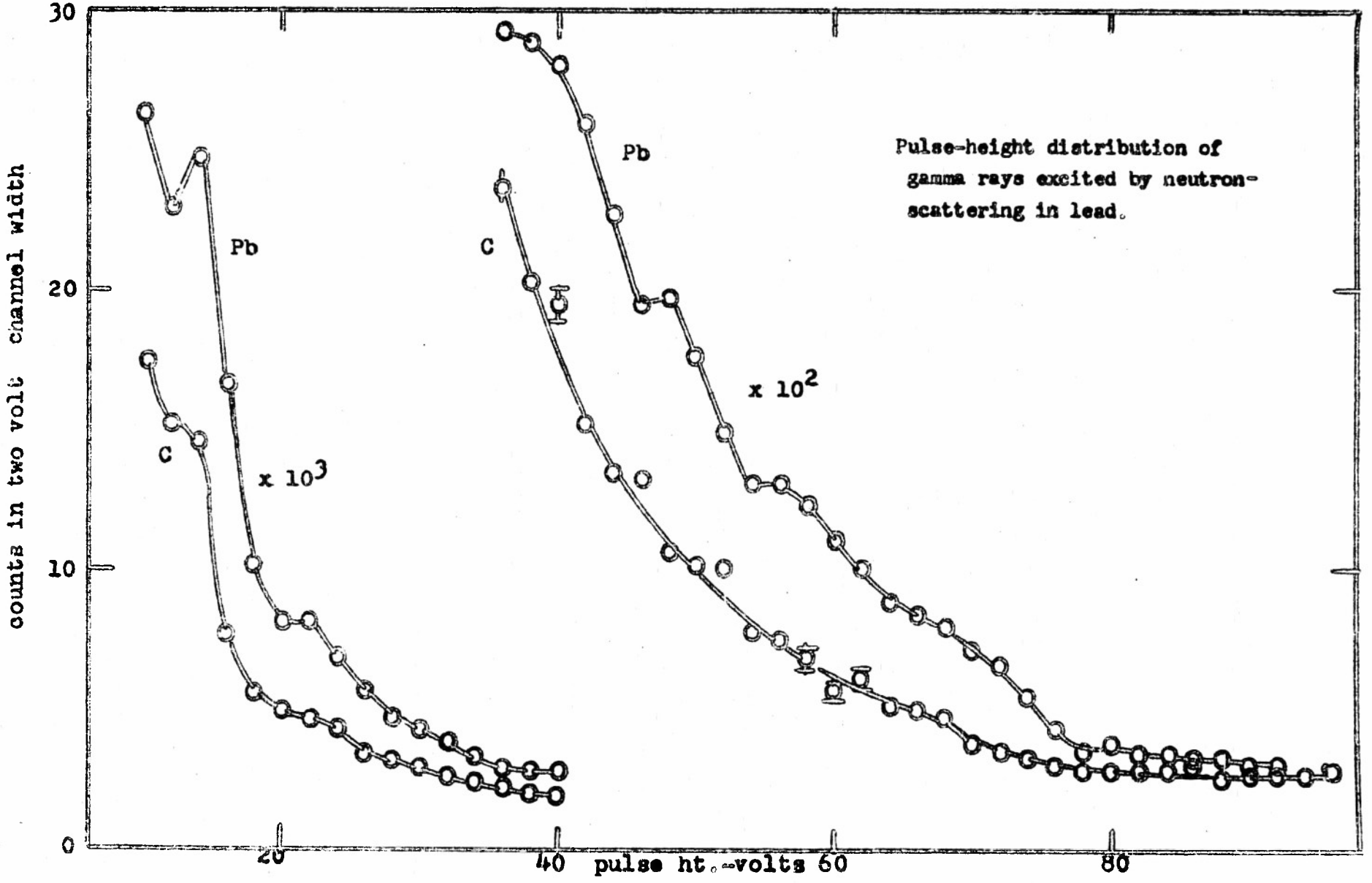
30
20
10
0
counts in two volt channel width
Pb
C
x 10³
Pb
C
x 10²
Pulse-height distribution of gamma rays excited by neutron-scattering in lead.
20
40
pulse ht.-volts
60
80

FIGURE 5

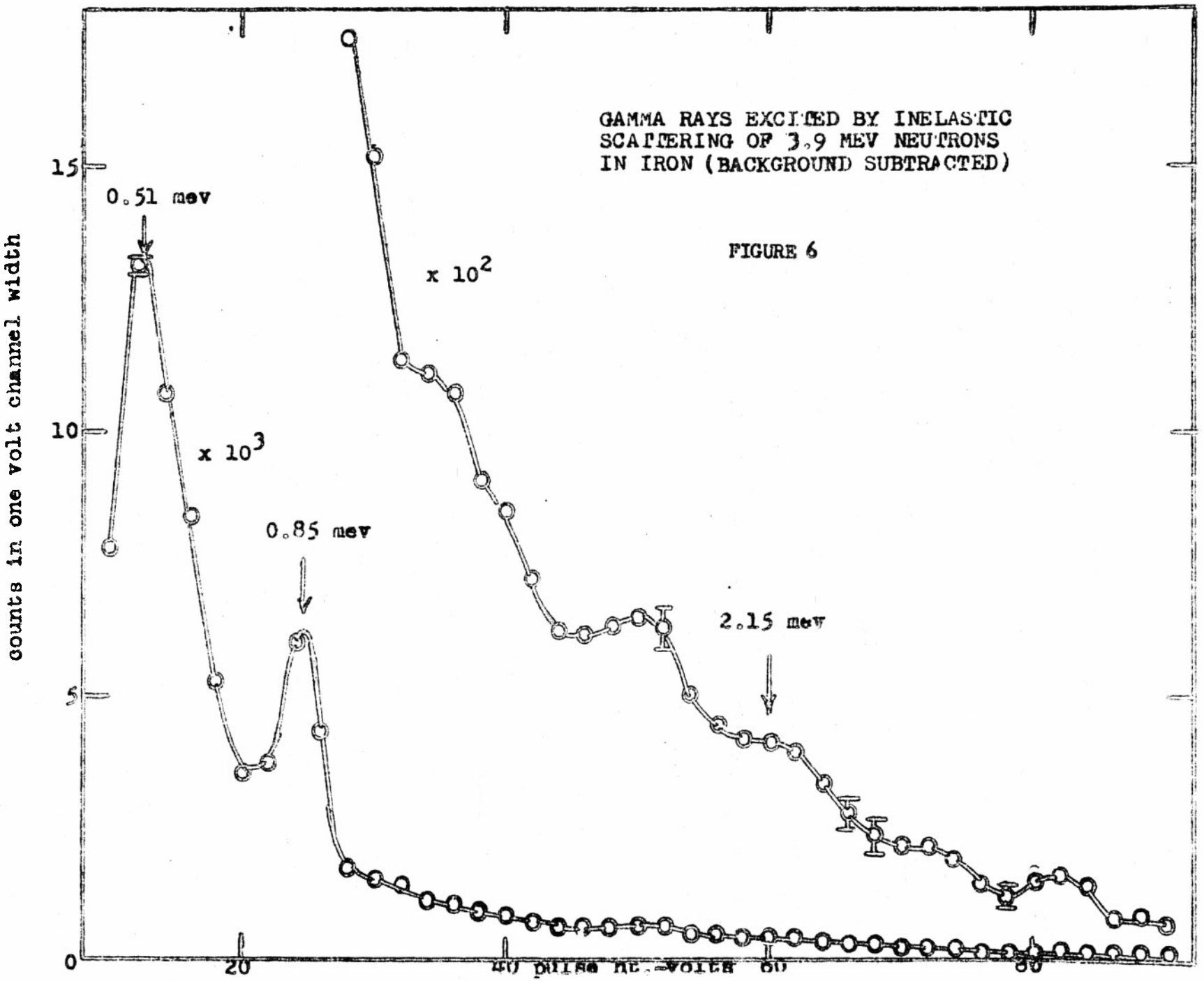
GAMMA RAYS EXCITED BY INELASTIC SCATTERING OF 3.9 MEV NEUTRONS IN IRON (BACKGROUND SUBTRACTED)
FIGURE 6
counts in one volt channel width
0.51 mev
0.85 mev
2.15 mev
x 10^2
x 10^3
15
10
5
0
20
60
80

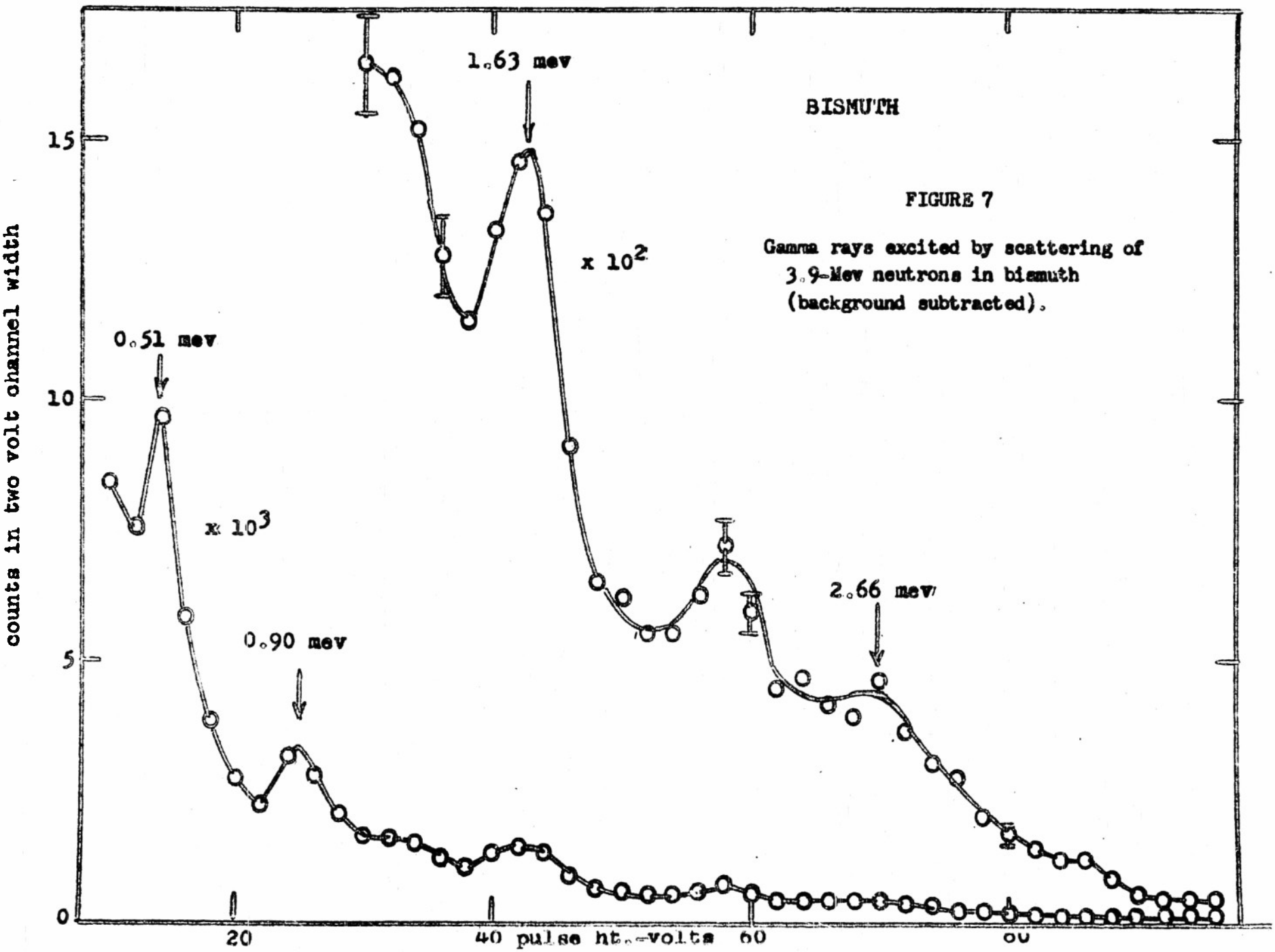


FIGURE 7

Gamma rays excited by scattering of 3.9-Mev neutrons in bismuth (background subtracted).

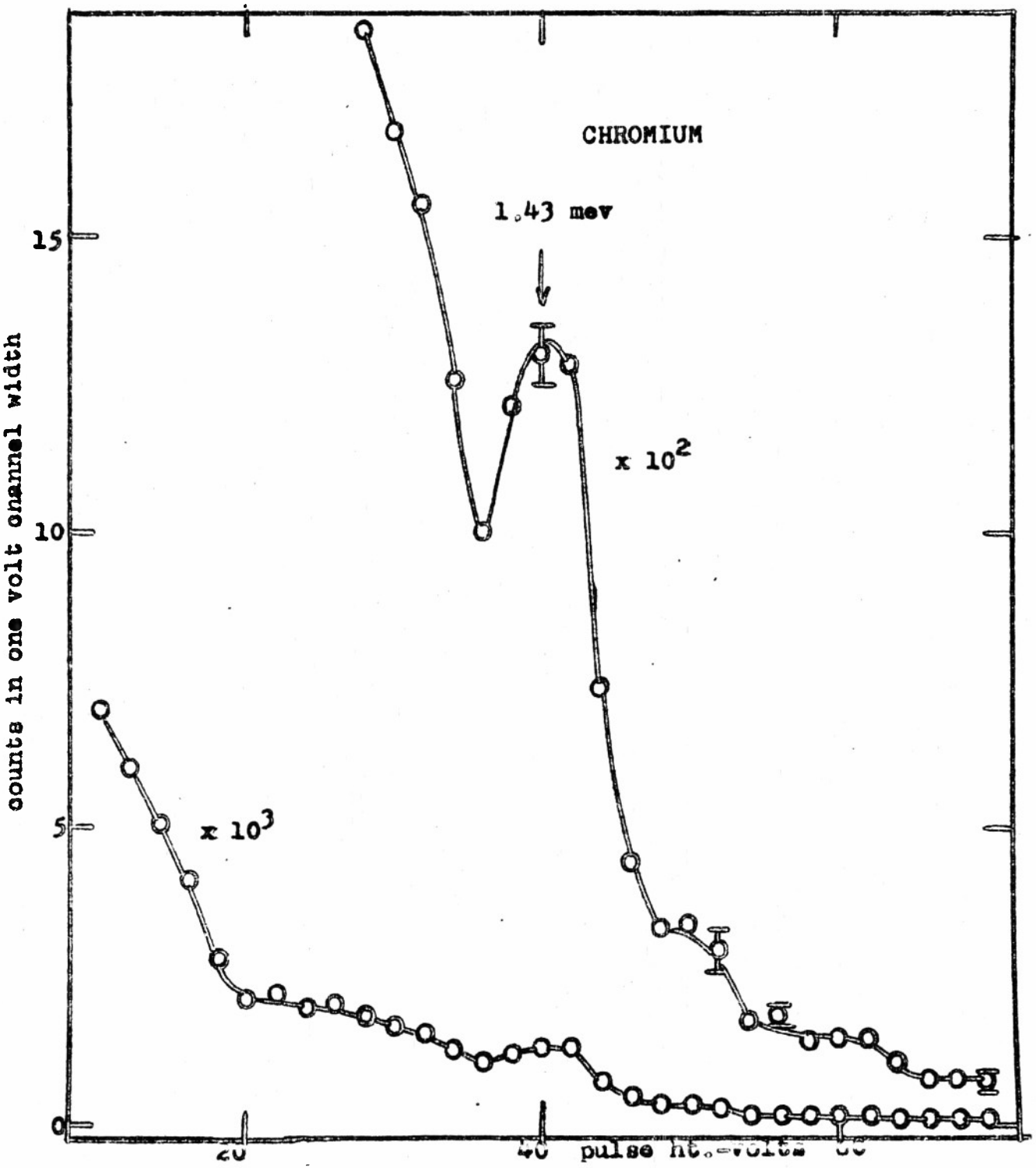


FIGURE 8

Gamma rays excited by scattering of 3.9-Mev neutrons in chromium (background subtracted).

The relative intensities of the gamma rays are per atom of element present per unit of neutron flux. Thus, the intensities can be compared among themselves, irrespective of element. For example, the ratio of the intensity of the 2.66 Mev gamma ray of lead to that of the 0.85 Mev gamma ray of iron is 450:680, if equal numbers of lead and iron atoms are irradiated by fast neutrons of energy 3.9-Mev. In arriving at the relative intensities of Table I, it was necessary to attempt to take into account the attenuation of neutrons and gamma rays in the ring scatterers. Several approximations are involved; so it is thought that the results are accurate only to a factor of 2 or 3.

The method of analysis of the gamma-ray spectra should now be considered. In Figure 10 is shown the gamma-ray spectrum of $Na^{24}$. This curve is readily interpretable. The photoelectric peak of the 2.76 Mev gamma ray is present, followed by escape peaks at 2.25 Mev and 1.74 Mev which are superposed upon the Compton distribution. The photoelectric peak of the 1.38 Mev radiation also appears and somewhat lower in energy is the associated Compton edge. The spectrum of $Na^{24}$ was observed with the radioactive source within the lead scattering ring in the geometry of Figure 3, outside the ring, and directly in front of the scintillation-counting crystal. The three spectra did not differ materially among themselves. They all resembled Figure 10 which was taken with the source of $Na^{24}$ in front of the crystal. The value of this curve in making an analysis is immediately

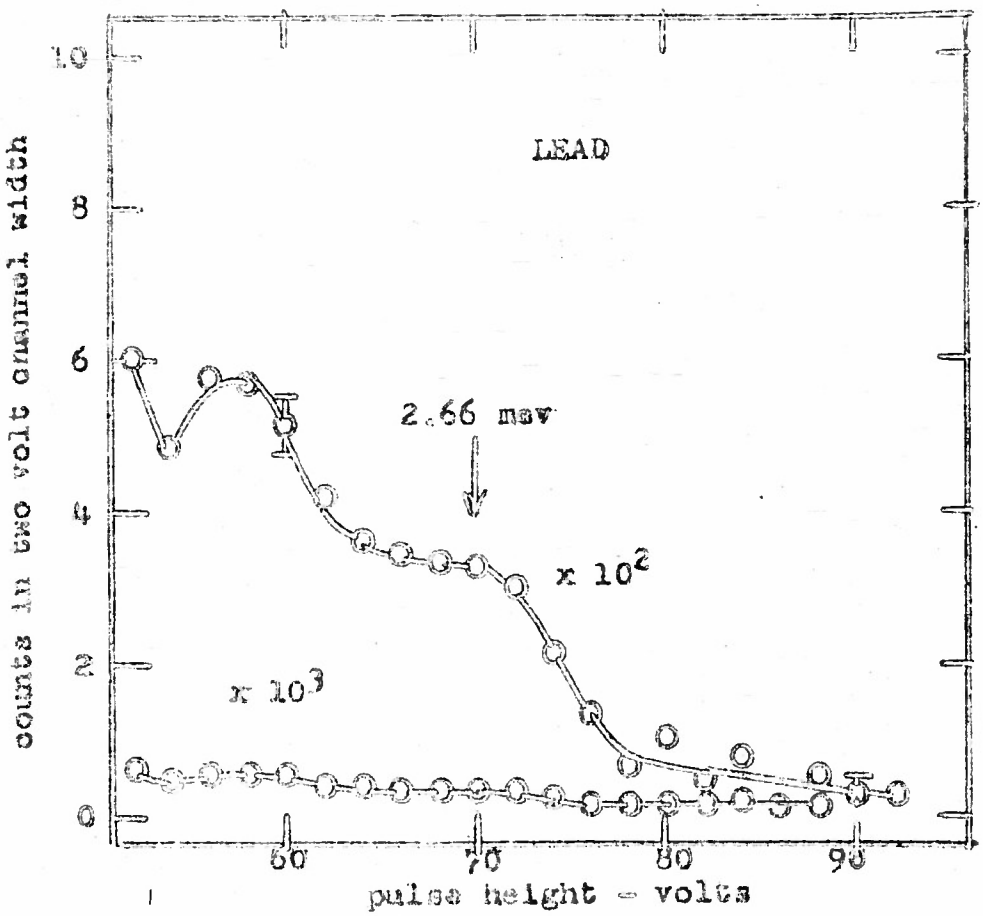


FIGURE 9

Gamma rays excited by scattering of 3.9-Mev neutrons in lead (background subtracted). This curve is obtained by treating the high energy region of Figure 5. Because of certain experimental uncertainties, the region of lower energy was not analyzed in detail for lead.

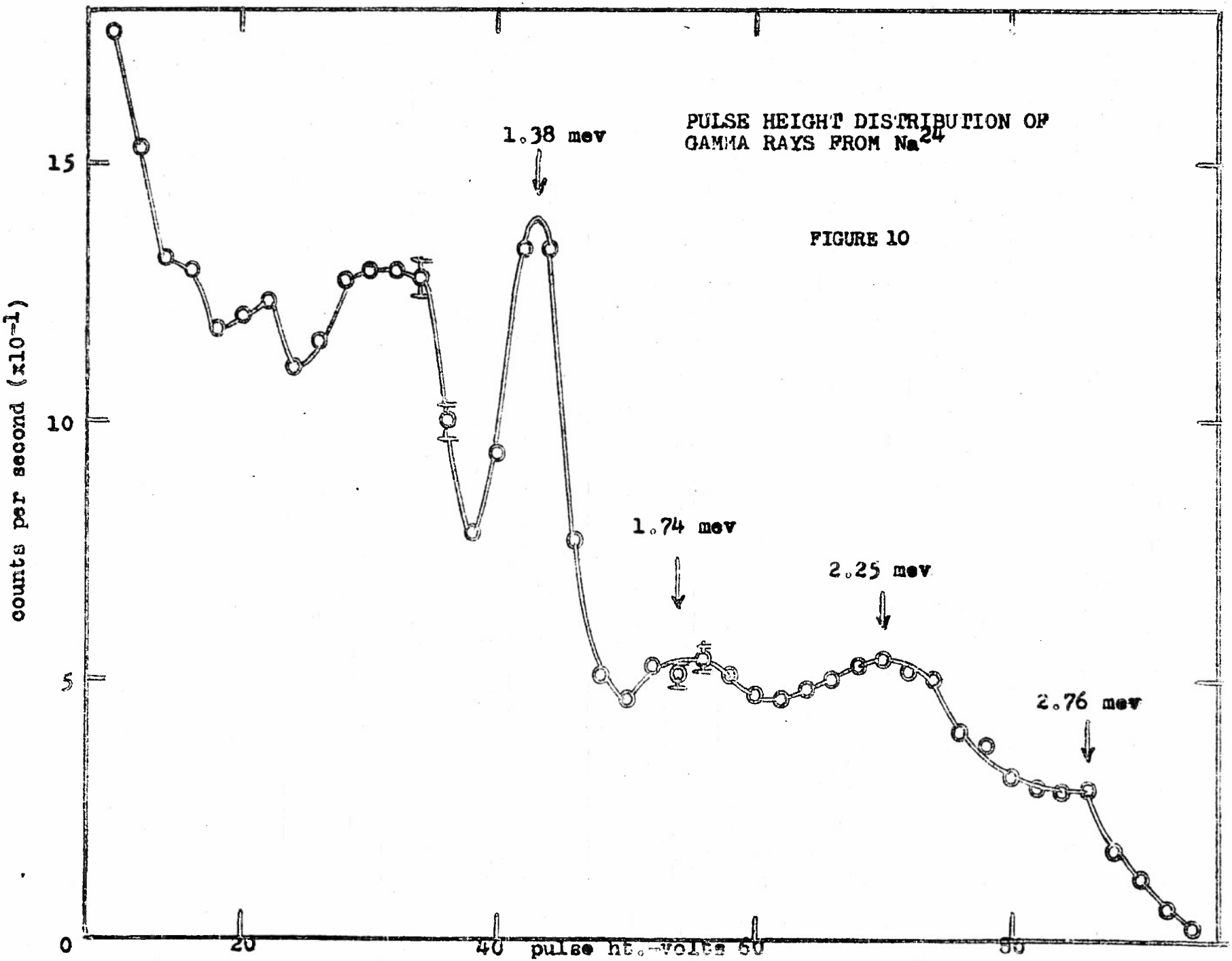
PULSE HEIGHT DISTRIBUTION OF GAMMA RAYS FROM $Na^{24}$
1.38 mev
1.74 mev
2.25 mev
2.76 mev
counts per second (x10-1)
15
10
5
0
20
40
pulse ht.-volts
50

FIGURE 10

evident. For example, the photoelectric peak and first escape peak of the 2.66 Mev gamma ray are clearly recognizable in Figure 9 on comparing them with the photo-peak and first escape-peak of the 2.76 Mev gamma ray of $Na^{24}$. Similar comparisons show that a 2.66 Mev gamma ray is excited in bismuth as shown in Figure 7. However, the high energy edge of the photo-peak does not drop off rapidly. Instead, it drops slowly, suggesting the presence of gamma radiation of higher energy. An indication of a photo-peak appears at $\sim$ 3.26 Mev. The gamma-ray spectrum of iron, given in Figure 6, exhibits peaks which are conservatively interpreted as two gamma rays having respectively energies of 0.85 Mev and 2.15 Mev. The peak lower in energy and adjacent to the photo-peak at 2.15 Mev is at present interpreted as an escape peak. Gamma rays of energies greater than 2.15 Mev are clearly present but are not specifically identified in energy. The bulk of the gamma radiation of chromium is evidently concentrated in a gamma ray at 1.43 Mev as shown in Figure 8. Gamma rays of higher energy are also present. The gamma ray of energy 1.43 Mev is thought to be emitted in $Cr^{52}$, and the gamma rays of higher energy are thought to be emitted from other isotopes of chromium. The relative isotopic abundance of $Cr^{52}$ is 82 per cent. The gamma rays of higher energy are thought not to be emitted from $Cr^{52}$, because the spin values of its energy levels make cross-over transitions of energies greater than 1.43 Mev very improbable. In Figures 6, 7, and 9, the spectra for iron,

bismuth, and lead, it is to be noted that an intensive gamma ray appears at 0.51 Mev. This is, of course, the annihilation radiation resulting from pair production by the high energy gamma rays within the ring scatterers themselves.

Returning to the photographic plate spectrum of Figure 2, it should be noted that although the 1.45 Mev gamma ray corresponds properly to the energy difference between the elastic group and the more energetic inelastic one, no gamma ray was detected corresponding to the energy difference between the two inelastic groups. The precise explanation for this discrepancy between the gamma ray and neutron measurements may have either of two forms:

1) The least energetic group of neutrons in the spectrum of Figure 2 may result from scattering of neutrons from the paraffin wedge into the chromium scatterer and thence to the photographic plates. The background run should have been taken with a carbon cylinder in place of the chromium cylinder. Instead, the background was simply collected with the chromium scatterer removed and nothing taking its place.

2) The gamma-ray spectrum of chromium rises steadily below 0.7 Mev. The counting rate is not immediately interpretable. The pile-up of counts in the region

of low energy may be related to scattered gamma radiation having its origin in various parts of the Van de Graaff statitron and obscuring the sought for gamma ray corresponding to the energy difference between the two inelastic groups of neutrons.

It is hoped that these several difficulties will be resolved in the near future.

## II. TOTAL CROSS SECTIONS; ANGULAR DISTRIBUTION OF ELASTIC SCATTERING; INELASTIC CROSS SECTIONS.

### Introduction

Measurements of the angular distribution of fast neutrons scattered from a large number of elements have been reported previously by Kikuchi and Aoki et al.[1], and Amaldi et al.[2] in which the main features of the distribution could be explained as the diffraction effects due to the scattering of neutron waves by spherical particles. More recently Remund and Ricamo[3] have measured angular distribution of 3.7 Mev neutrons scattered from carbon while Walt and Barschall[4], using 1.00 Mev neutrons have reported the angular distributions for a large number of elements. Feshback, Porter and Weisskopf[5], using a modification of the continuum theory of nuclear reactions, have reproduced the average features of the total neutron cross section versus energy and atomic number as measured by Barschall[6]. Feshback, Porter, and Weisskopf[7] have also computed the angular distributions of elastically-scattered neutrons using this same modification of the continuum theory and the general features agree rather well with the measurements of Walt and Barschall[4]. Our measurements on aluminum, iron and lead, using 3.7 Mev neutrons, were undertaken with the thought that the angular distribution in this energy range would be of value in view of the present theoretical considerations.

### Experimental

Figure 1 shows the experimental arrangement that was used to measure the angular distribution of neutrons scattered from

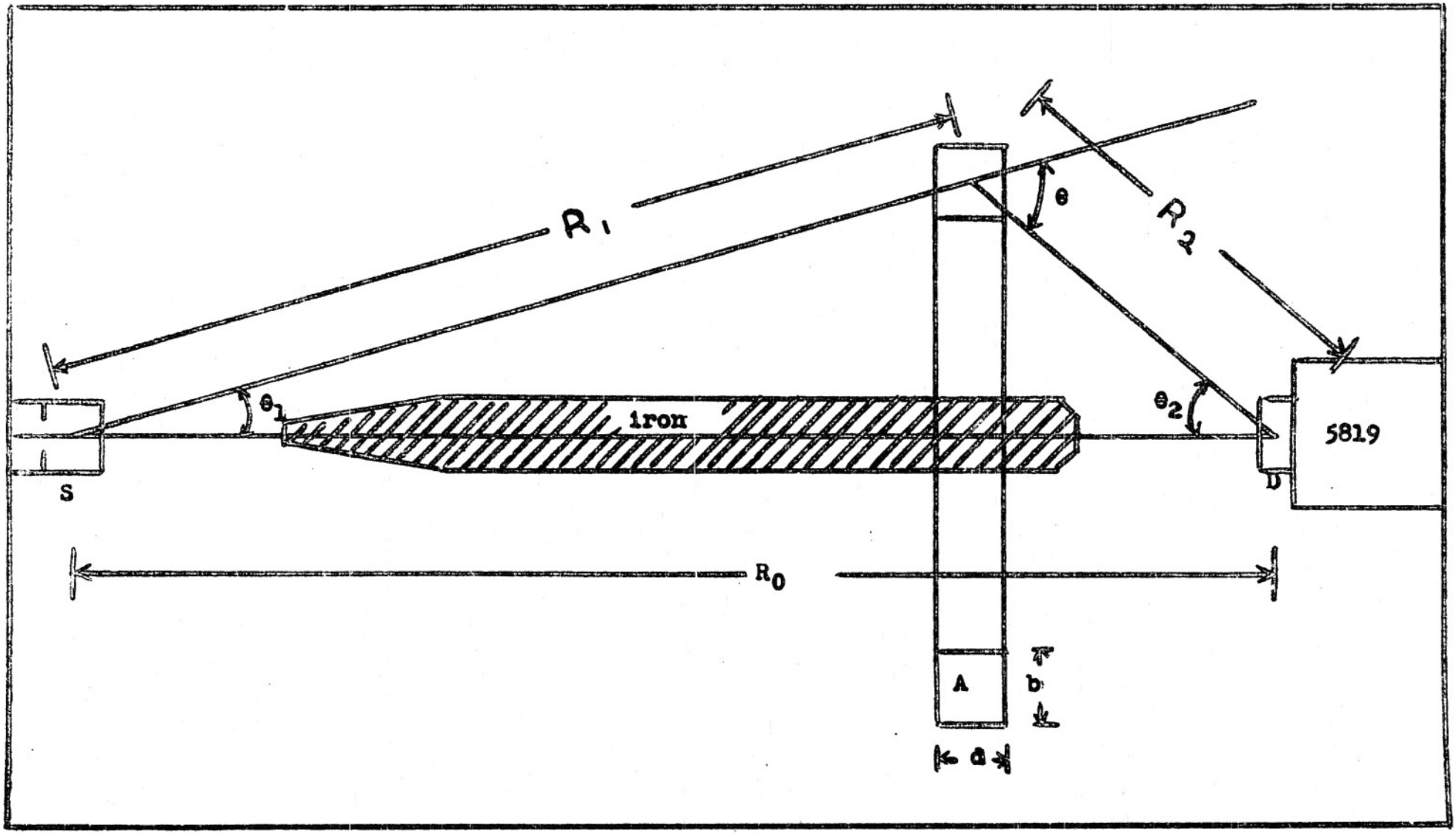


FIGURE 1. Ring geometry for scatterer, (S), deuterium gas at one-half atmosphere pressure to give neutrons of about 3.7 Mev; (D) Lucite-zinc sulphide scintillation detector; (A) ring scatterer of rectangular cross section.

aluminum, iron and lead. The source of neutrons is a chamber of deuterium gas at 0.5 atmosphere and 2.0 cm in depth bombarded with about 10 microamperes of 1.0 Mev deuterons which after passing through the nickel foil and gas have a mean energy of about 0.65 Mev. These neutrons are detected by a pressure molded Lucite-zinc sulphide button[8] mounted directly on the face of an RCA 5819 photomultiplier. The direct beam is cut out by a suitably tapered 10 inch long, 1 1/8 inch diameter iron cylinder. The scatterer was chosen to have the shape of a ring in order to increase as much as possible the number of scattered neutrons. The scattering angle $\Theta$ is varied by moving the scattering rings laterally, and by using rings of various sizes. For angles between 52° and 140° degrees, 8 inch O.D. rings were used with a mean source-detector distance $R_o$ of 40 cm. For $\Theta$ between 24 degrees and 52 degrees, 6 O.D. inch rings were used with $R_o$ equal to 60 cm. For the point at 15°, 4" O.D. rings were used with $R_o$ equal to 72 cm.

In order to discuss the measurements that must be made to arrive at the differential scattering cross section, it is convenient to define several quantities. For a given number of neutrons emitted by the neutron source, let $N_S$ be the number of neutrons recorded by the detector with the scatterer and direct beam attenuator in place. Let $N_B$ be the number of neutrons detected with the scatterer removed and let $N_D$ be the number of neutrons recorded with the scatterer and attenuator removed. The $N_S-N_B$ is the number of scattered neutrons recorded by the detector that originate in the source, and $N_D-N_B$ is the number

of neutrons direct from the source that are recorded by the detector. Let the scattering ratio be defined as

$$S \equiv (N_S - N_B)/(N_D - N_B).$$

Appendix I then shows that the scattering ratio S is related to the apparent differential scattering cross section $\bar{\sigma}(\Theta)$ through the relation

$$S = \left[I(\theta_1)/I(0)\right] \cdot \left[R_o^2/R_1^2 R_2^2\right] \cdot \bar{\sigma}(\theta) A(\theta_2) E(E_n) nV F(\theta_2) \exp(-\sigma nd) \qquad (1)$$

where $I(\theta_1)$ is the number of neutrons emitted from the source per steradian per unit monitor flux, $A(\theta_2)$ is the angular sensitivity of the neutron detector normalized to unity at zero angle, $E(E_n)$ is the energy sensitivity of the neutron detector normalized to unity for the energy of the direct beam, nV is the number of scattering nuclei, $\sigma$ is the total scattering cross section, and $F(\theta_2)$ is an attenuation factor which is defined more fully in Appendix I.

In general, the scattering ratio S is made up of a sum of terms $S = S_1 + S_2 + \text{etc.}$, where $S_1$, $S_2$, etc. refer to the neutrons scattered into the detector by single scattering, double scattering, etc. Thus, $\bar{\sigma}(\Theta)$ is simply a measure of the differential scattering cross section, assuming that all neutrons are singly scattered, since $\bar{\sigma}(\Theta)$ becomes exactly

$\sigma(\Theta)$ if S is replaced by $S_1$. In order to separate the components $S_1$, $S_2$, etc., one measures the scattering ratio S for a fixed angle $\Theta$ as a function of the axial thickness of the ring scatterer d. The value of $\sigma(\Theta)$ at d = 0 is then the average differential scattering cross section for all scattered neutrons (elastic and inelastic) weighted according to the energy sensitivity of the detector $E(E_n)$. In the ideal case, if the energy sensitivity curve adequately discriminates against the inelastically scattered neutrons, the above value of $\sigma(\Theta)$ for d = 0 becomes the differential cross section for elastic scattering $\sigma(\Theta)$.

In order to measure $\bar{\sigma}(\Theta)$ it is necessary to consider the following factors.

1. Energy resolution of incident neutrons. The mean energy of the neutrons incident on the scatterer varies between 3.70 Mev and 3.74 Mev depending on the angle $\theta_1$. The energy spread in the beam due to target thickness and voltage stability of the generator is about 200 Kev.

2. Neutron flux monitor. A proportional counter filled with one atmosphere of butane was placed very close to the target chamber at 90 degrees with respect to the source-detector axis. The discriminator was set to reject those neutrons that were produced from the $C^{12}(d,n)$ reaction in the vicinity of the magnet box. Actually, some difficulty was experienced in obtaining a constant direct beam neutron count per unit monitor count after the target chamber was just filled

with deuterium. The pattern of change, however, was similar in each case and seemed to indicate that some of the deuterium gas was absorbed into the walls of the chamber. After about an hour or two a ratio was obtained that was constant to $\pm$ 5 per cent.

3. Measurement of S. In general, the direct beam count was about 15-100 times the scattered beam count and the attenuated direct beam count varied from 40 per cent to 90 per cent of the scattered beam count, each depending on the size and position of the scatterer.

4. Spacial distribution of neutron source. The $N_D - N_B$ count exhibited within a few per cent an inverse square variation with distance from the target chamber.

5. Angular variation of the neutron flux from the D-D reaction. $I(\Theta_1)/I(0)$. This quantity was computed from the data published by Hunter and Richards[9].

6. Measurement of nV. the number of scattering nuclei. Each scatterer was weighed on a suitable balance to about one per cent accuracy.

7. Angular variation in sensitivity of the neutron detector. $A(\Theta_2)$. This quantity varied by about 25 per cent over the range of $\Theta_2$ used in this experiment. The value of $A(\Theta_2)$ was measured to within about 5 per cent by rotating the

detector about an axis through the detector perpendicular to the source-detector axis.

8. Measurement of the total cross section . This was measured by using 1 1/8 inch diameter, 1 inch long cylinders of aluminum, iron and lead. The cross sections obtained for $E_n$ = 3.7 Mev were $\sigma$(Al) = 2.55 barns, $\sigma$(Fe) = 3.51 barns, and $\sigma$(Pb) = 7.60 barns each in agreement with the values obtained by Neresen and Darden[10]. The scattering-in corrections were 0.75, 2.4, and 4.3 per cent, respectively, for Al, Fe and Pb, and were obtained from our measurements of the differential cross section.

9. The attenuation factor, F. This factor varied from unity by as much as 14 per cent depending on the size and shape of the scatterer. This quantity is discussed briefly in Appendix I and a graph of its variation is given in Fig. 2.

10. Geometrical Measurements. Measurements of distance were carried out to about ± 1 millimeter. The consequent calculation of mean angles is thus accurate to about one per cent. However, because of the finite size of the detector (1 inch diameter, 5/8 inch height) and the finite size of the scatterers, the detected neutrons are received over a range of angles of about ± 10 degrees in the worst case near $\Theta$ = 90 degrees.

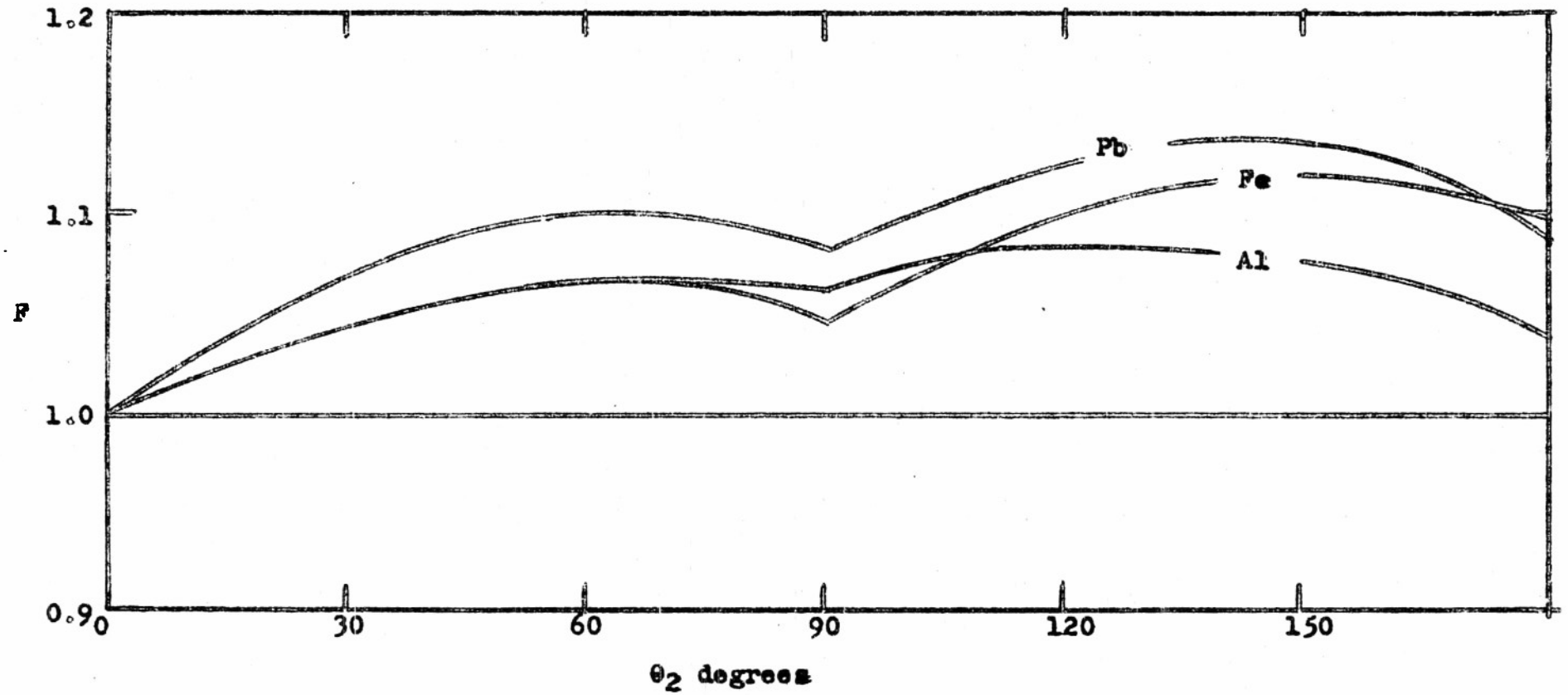


Figure 2. Attenuation factor F. This quantity is defined in Appendix I. F exp(- σnd) essentially measures the attenuation of the direct beam into the scatterer times the attenuation of the scattered beam out of the scatterer. The dimensions are for aluminum, iron and lead: b = 2.54 cm, 2.54 cm and 2.54 cm; d = 3.15 cm, 2.54 cm, and 3.00 cm. The factor F is not shown for the thinner rings used in the experiment.

11. Variation of the sensitivity of the detector with neutron energy. This was measured by comparing our measurement of the angular distribution of neutrons from the D-D reaction with those of Hunter and Richards[9], the discrepancy being ascribed to a non-uniform efficiency in our detector. As may be seen in Fig. 3, the sensitivity only drops off slowly with decreasing neutron energy, decreasing by 40 per cent in 1 Mev. Since it is desired to discriminate against neutrons that have lost more than 200 Kev, this constitutes a serious objection to the use of the Lucite-zinc sulphide detector in this experiment. However, if the inelastically scattered neutrons are more uniformly distributed in angle than the elastically scattered neutrons, then the general features of the differential cross section for elastic scattering will still be evident. In any case the value obtained for $\sigma(\Theta)$ must be such that the total cross section gotten by integrating $\sigma(\Theta)$ is less than the measured total cross section. That this is the case will be shown later.

12. Sensitivity of counter to gamma rays. Neutron detector must not count the gamma rays resulting from the inelastic scattering of neutrons. An ampoule containing 0.1 milligram of radium was placed directly on the Lucite-zinc sulphide detector and gave a negligible counting rate (less than 1 count in 100 seconds).

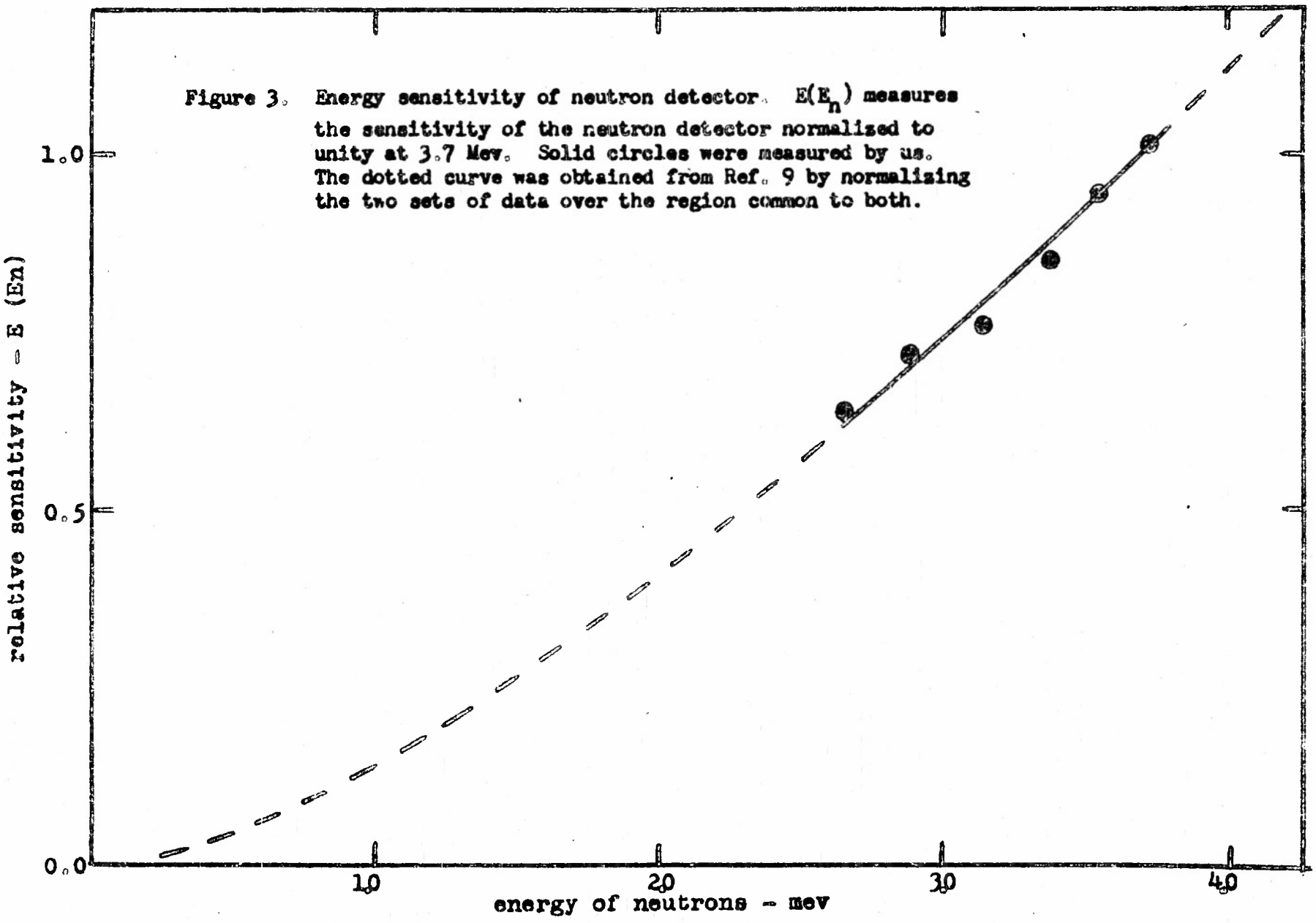


Figure 3. Energy sensitivity of neutron detector. $E(E_n)$ measures the sensitivity of the neutron detector normalized to unity at 3.7 Mev. Solid circles were measured by us. The dotted curve was obtained from Ref. 9 by normalizing the two sets of data over the region common to both.

13. Higher order scattering. Appendix II gives an account of the method used in this experiment to allow for double scattering. Essentially it involves placing an upper and lower bound on the possible values of $\sigma(\Theta)$ for an observed sequence of values of $\bar{\sigma}(\Theta)$ as a function of the axial thickness of the ring. The first calculation estimates the nature of the variation of $\bar{\sigma}(\Theta)$ with d/a under the assumption of isotropic scattering. This is given by Eq. (13) which, after comparing with Fig. 4, is seen to reduce to the practical formula

$$\bar{\sigma}(\Theta) = \bar{\sigma}_o(\Theta) - .282\,\bar{\sigma}'(\Theta) \qquad (2)$$

where $\bar{\sigma}_o(\Theta)$ is the intercept at d/a = 0 of the linear portion of the curve and $\bar{\sigma}'(\Theta)$ is the slope of the $\bar{\sigma}(\Theta)$ versus d/a curve in the linear portion.

The second calculation states that if the angular distribution is peaked strongly forward, then one expects that the double scattering contribution will cause $\bar{\sigma}(\Theta)$ to be a linear function of d or d/a. In this case $\bar{\sigma}_o(\Theta)$ is the true differential scattering cross section. Both of these extrapolations are presented on the graphs.

If triple scattering is present, than $\bar{\sigma}(\Theta)$ should be a quadratic function of d or d/a for the case in which there is a strong forward peaking of the scattering. Figure 5 for

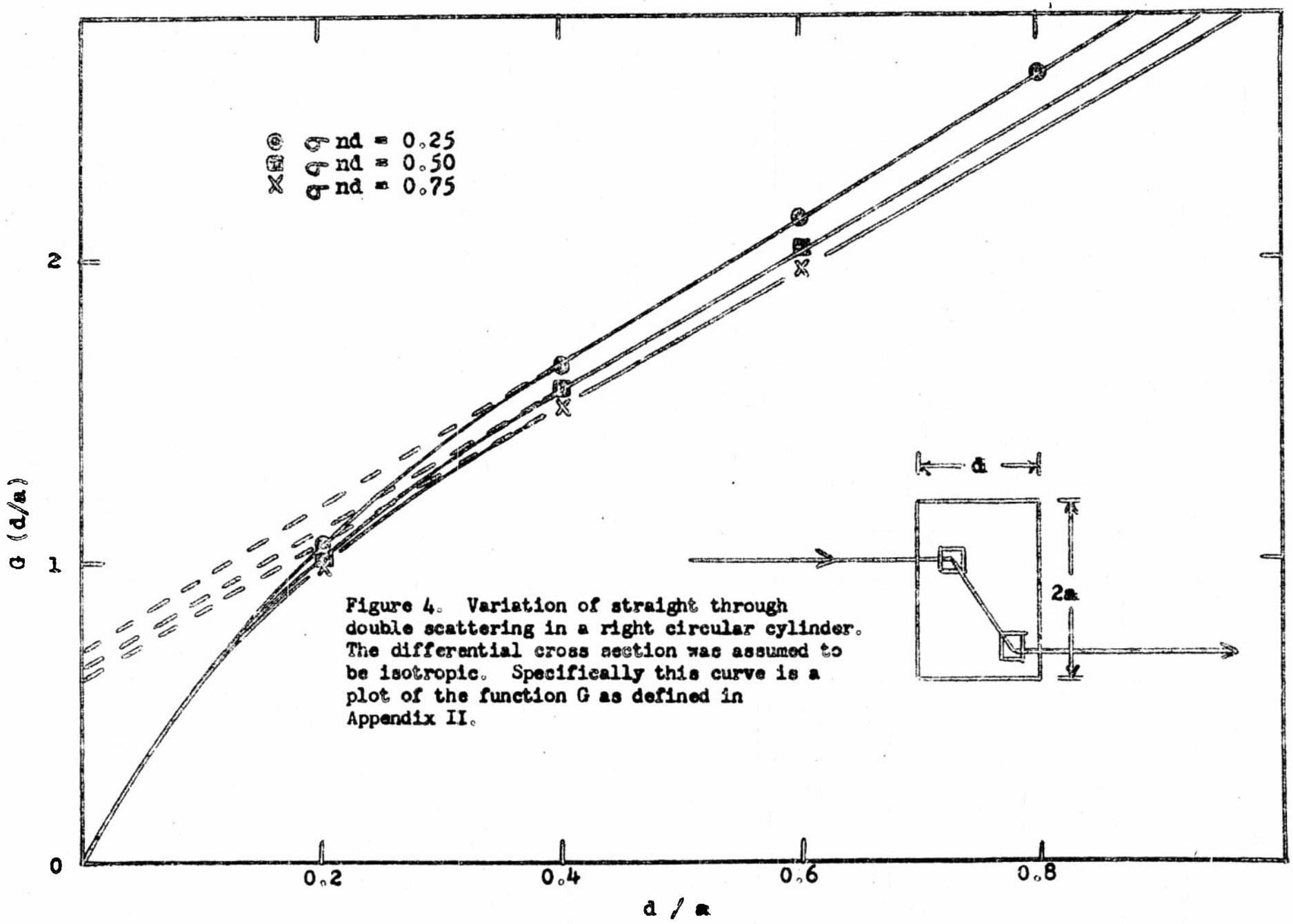


Figure 4. Variation of straight through double scattering in a right circular cylinder. The differential cross section was assumed to be isotropic. Specifically this curve is a plot of the function G as defined in Appendix II.

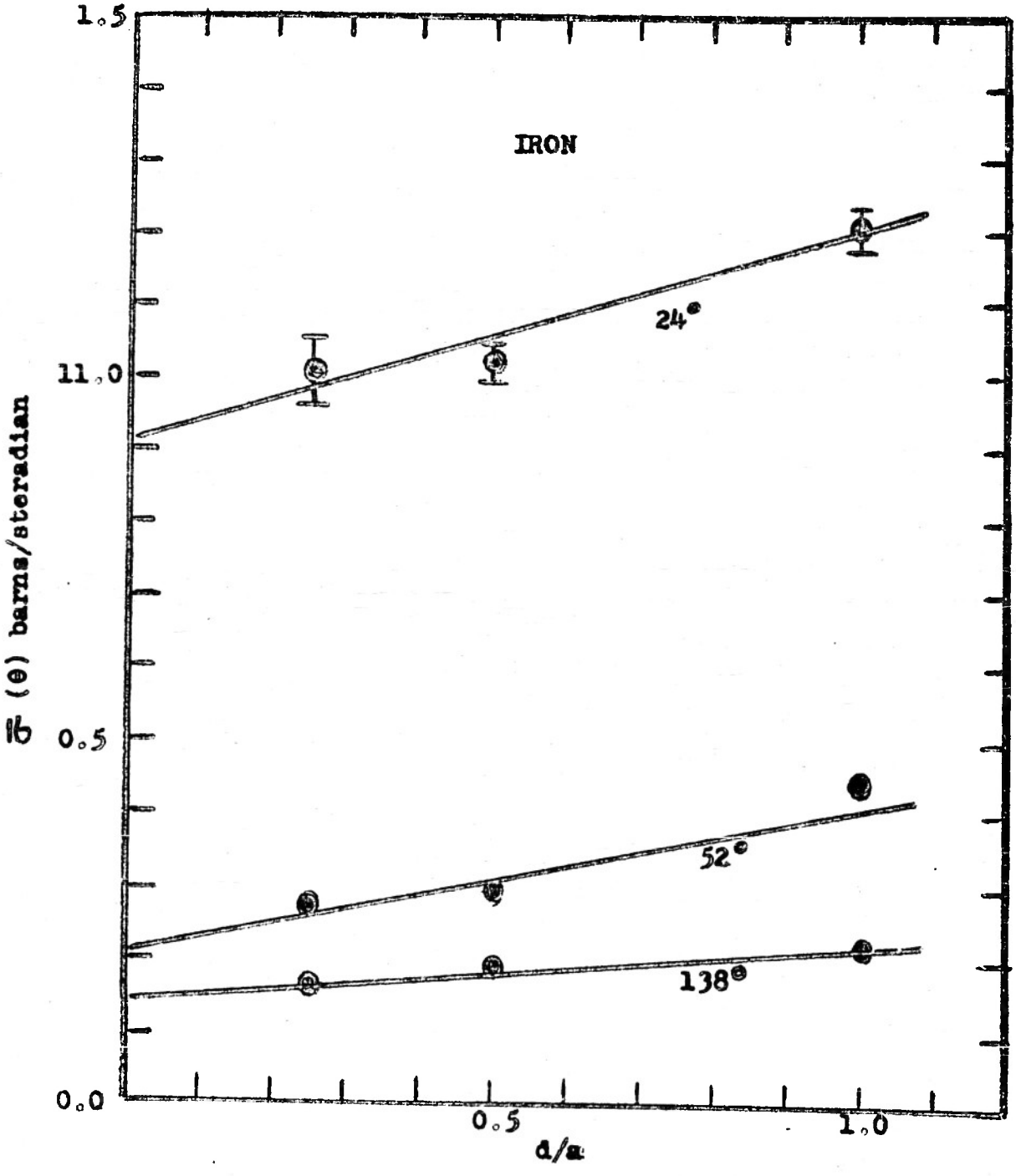


FIGURE 5.

Apparent differential cross section of iron versus thickness of ring scatterer for three different scattering angles. The thickness is measured relative to a quantity a, which we have taken to be equal to the radial width of the ring in order to establish a correspondence between the ring scatterer and the right circular cylinder scatterer.

the case of iron shows some indication of the presence of triple scattering, however, the experimental uncertainty is too large to consider this definite. No attempt was made to remove the triple scattering contributions.

A typical run of data was made as follows: (1) direct beam; (2) attenuated beam; (3) scattered beam from one of the rings for all values of the scattering angle; (4) attenuated beam; (5) direct beam. If the two values of the direct beam determination differed by more than 10 per cent, the data were discarded.

## DATA

Figures 6, 7, and 8 show the experimental points of the apparent differential cross section for 3.7 Mev neutrons incident on aluminum, iron, and lead as calculated from Eq. (1). Only a limited number of angles were chosen in order to determine the effects of higher order scattering. Figure 5 shows the variation of $\bar{\sigma}(\theta)$ as a function of the ring thickness for the case of iron. In the same manner, similar curves were obtained for lead and aluminum. The extrapolations both for isotropic scattering and forward peaked scattering are shown in Figures 6, 7, and 8 where a curve is drawn through the points thought to be the appropriate differential cross section, $\sigma(\theta)$ for each case. The total cross sections corresponding to $\sigma(\theta)$ have been calculated and are presented together with the measured total cross section in Table I. It will be noted that the integrated differential

FIGURE 6. Angular distribution of 3.7 Mev neutrons scattered from aluminum. $\bar{\sigma}(\theta)$ is apparent differential cross section as defined in the text. $\bar{\sigma}_o(\theta)$ is the differential cross section using a linear extrapolation to remove higher order scatters. $\bar{\sigma}_o(\theta) = .282\,\sigma''(\theta)$ is the differential cross section in which the higher order scatters are removed using the isotropic scattering assumption. $\sigma(0)$ is taken from the Final Report of the Fast Neutron Data Project, NYO-636, in which the nuclear radii were found from our measured values of the total cross section.

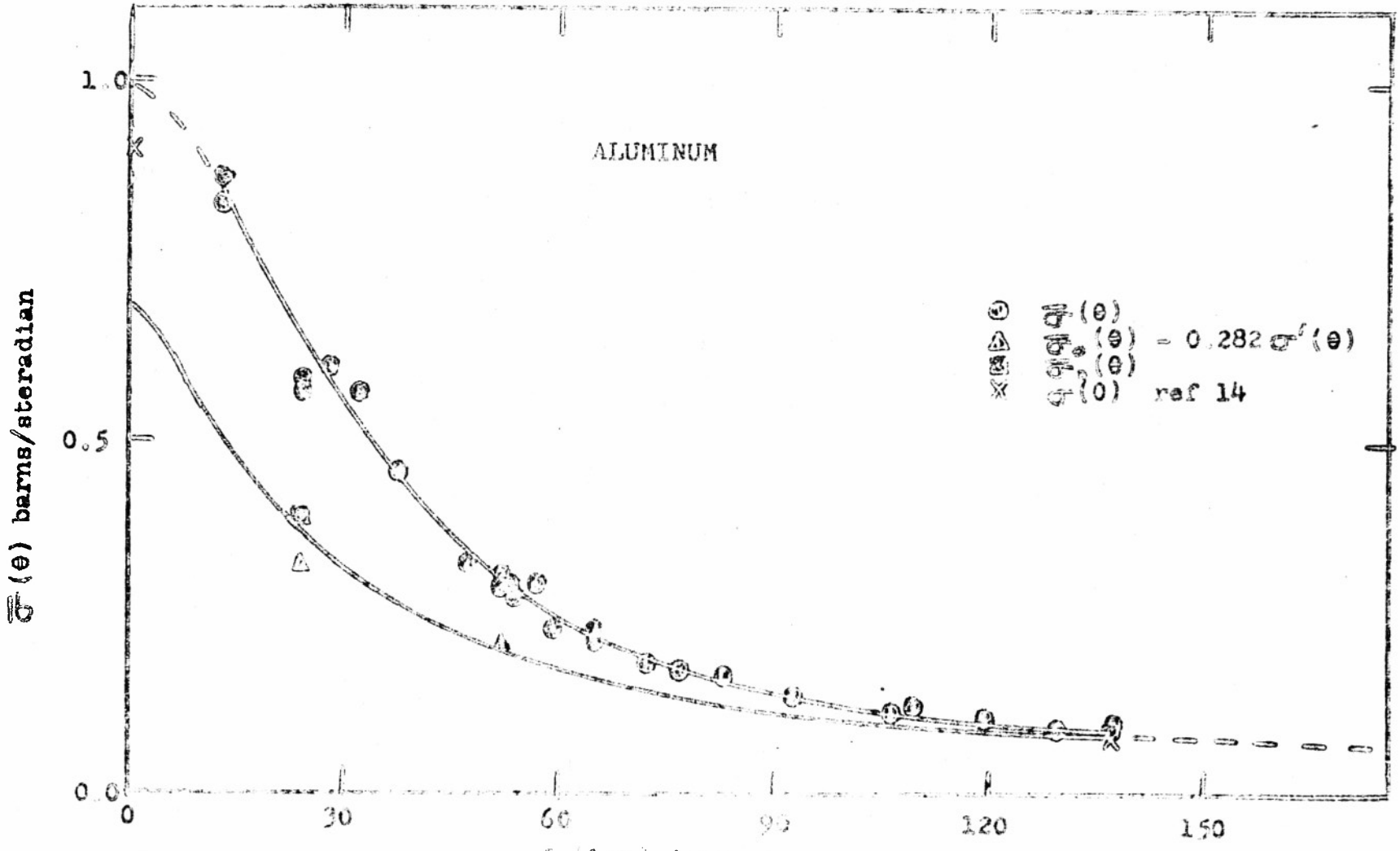

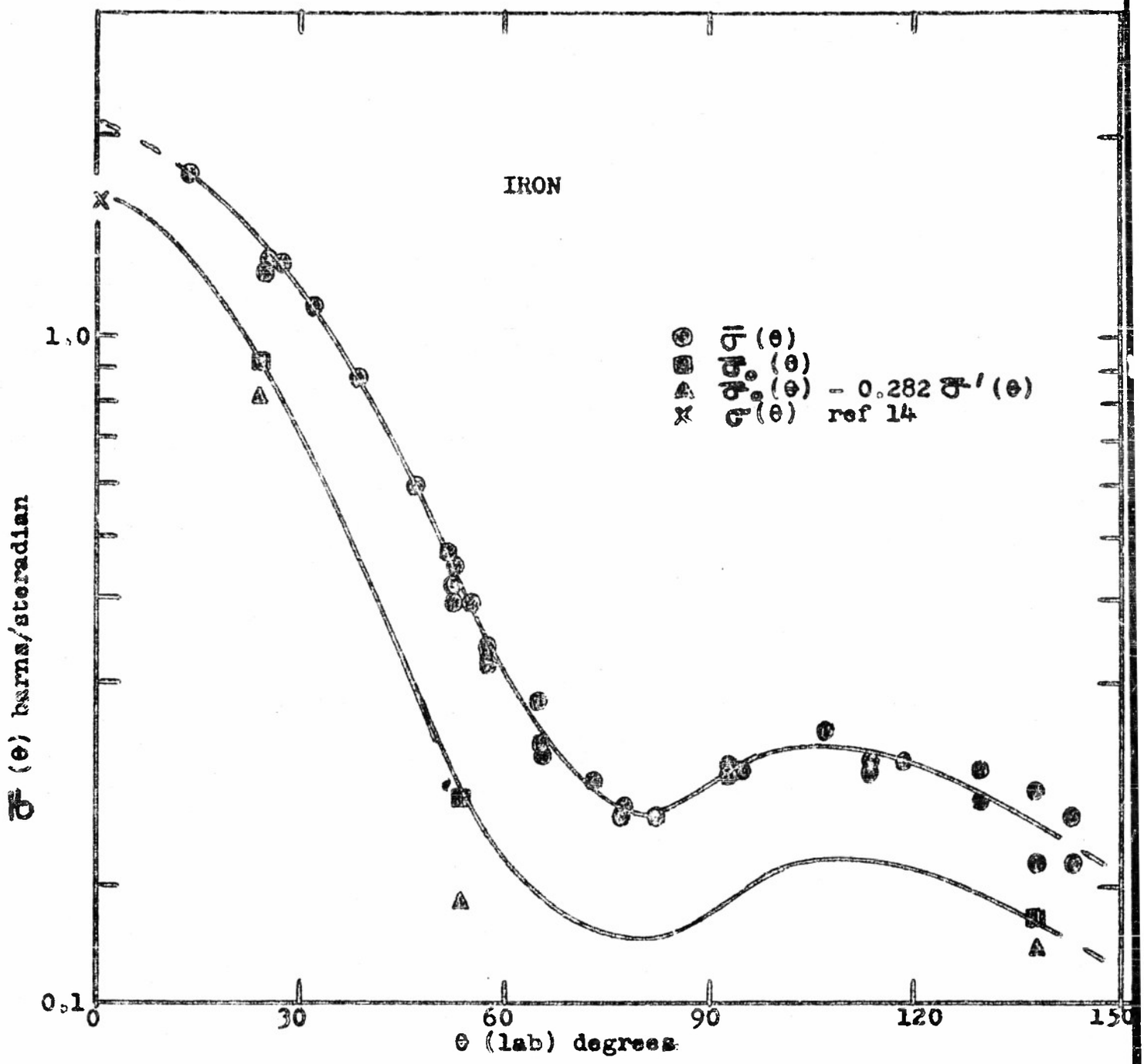


FIGURE 7. Angular distribution of 3.7 Mev neutrons scattered from iron. Other remarks in caption of Fig. 6 apply here also.

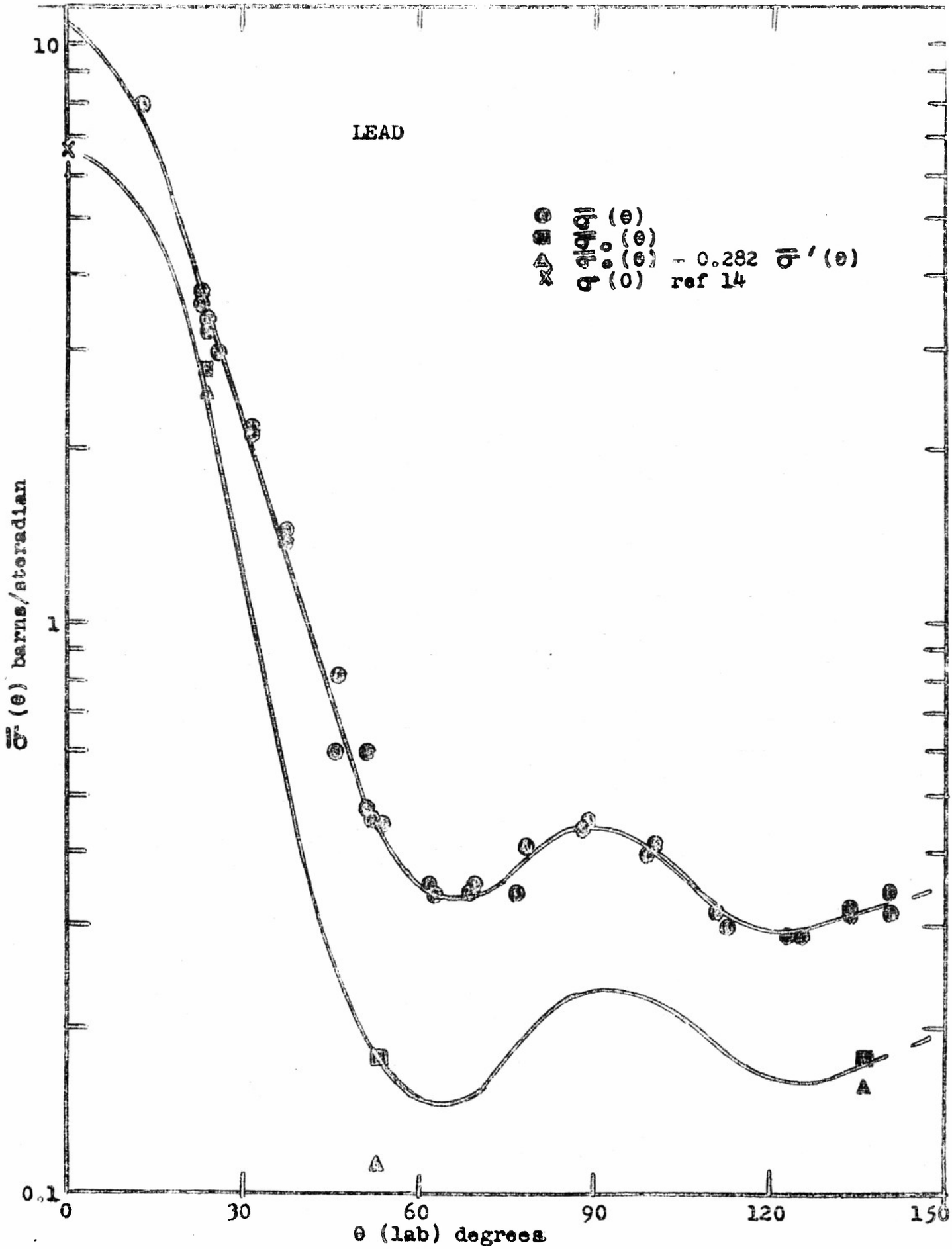


FIGURE 8. Angular distribution of 3.7 Mev neutrons scattered from lead. Other remarks in caption of Fig. 6 apply here also.

TABLE I.

| Element | $\sigma_{total}$ (measured) in barns | | $\int \sigma(\theta) d\Omega_\theta$ (barns) | $\sigma_I$ |
|---|---|---|---|---|
| | This Expt. | Neresen and Darden | | |
| Aluminum | 2.55 | 2.50 | 1.73 | 0.82 |
| Iron | 3.51 | 3.55 | 2.94 | 0.57 |
| Lead | 7.60 | 7.70 | 5.17 | 2.43 |

Total cross sections. The value of $\int \sigma(\theta) d\Omega_\theta$ subject to the reservations in the text is the total elastic cross section.

cross sections in each case is less than the measured total cross section. The total inelastic cross section cannot be obtained as the difference between the two former cross sections since the measurement of the differential cross section did not discriminate adequately against the inelastically scattered neutrons. However, this subtraction can be carried out approximately if one accepts the following rather crude estimate of the inelastic contribution to $\sigma(\theta)$: There are seven levels in aluminum that can be excited by 3.7 Mev neutrons[11]. If we assume that the maximum total inelastic cross section is about 50 per cent of the total cross section, and that the seven levels in aluminum are equally excited, then the inelastic neutrons contribute less than 15 per cent to the total cross sections corresponding to $\sigma(\theta)$. Similar arguments using the known levels in iron and lead show that the inelastic contribution in these elements is less than 20 per cent.

## APPENDIX I. SCATTERING OF NEUTRONS THROUGH RING SCATTERER BY SINGLE SCATTERING.

In general, the scattering rationis made up of a sum of terms $S = S_1 + S_2 + \cdots\cdots$ where $S_1$, $S_2$, etc. refer to the neutrons scattered into the detector by single scattering, double scattering, etc. For the single scattering case (Figs. 1 and 9a) we have

$$S_1 = \int_V \left[I(\theta_1)/I(0)\right] \cdot \left[R_0^2/R_1^2R_2^2\right] \cdot \sigma(\theta) n \exp\left[-\sigma n(r_1 + r_2)\right] \cdot A(\theta_2)E(E_n)dV \quad (3)$$

The geometry is such that only small errors will be introduced if Eq. (3) is replaced by

$$S_1 = \left[I(\theta_1)/I(0)\right] \cdot \left[R_0^2/R_1^2R_2^2\right] \cdot \sigma(\theta) n A(\theta_2)E(E_n)VF(\theta_2)\exp(-\sigma nd) \quad (4)$$

where

$$F = V^{-1}\int_V \exp\left[-\sigma n(r_1 + r_2 - d)\right] dV \quad (5)$$

and the mean angles and distances are used for $\theta_1$, $\theta_2$, $R_0$, $R_1$, and $R_2$. For a fixed size of ring scatterer, the quantity F is a function of $\theta_1$ and $\theta_2$. However, since $\theta_1$ only varies from

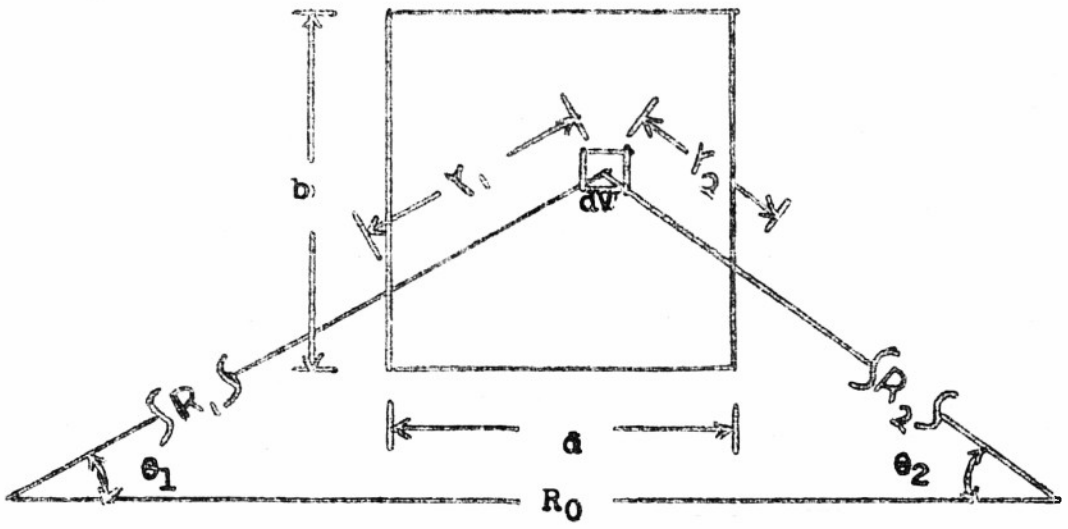


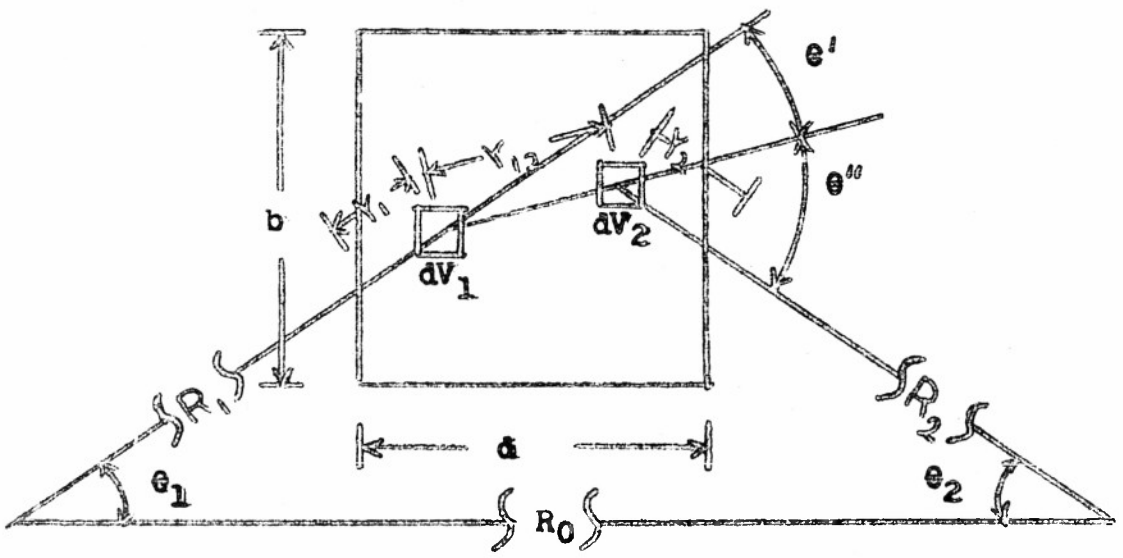


FIGURE 9. DETAIL OF SCATTERING GEOMETRY: (a) single scattering; (b) double scattering.

about $5^{\circ}$ to $15^{\circ}$, little error and much simplification is introduced by computing F for $\theta_1 = 0$. For the rectangular cross section of our scatterer, the integral F may be evaluated in terms of elementary functions. The results are displayed in Figure 2.

If only single scattering were present, the quantity $S_1$ could be replaced by the measured data S and the differential cross section $\sigma(\theta)$ could be calculated. In any case the reduction of the data is facilitated by defining an effective single scattering differential cross section $\bar{\sigma}(\theta)$ such that

$$S = \left[I(\theta_1)/I(0)\right] \cdot \left[R_o^2/R_1^2 R_2^2\right] \cdot \bar{\sigma}(\theta) n A(\theta_2) E(E_n) V F(\theta_2) \exp(-\sigma n d) \qquad (6)$$

APPENDIX II. SCATTERING OF NEUTRONS THROUGH RING SCATTERER BY DOUBLE SCATTERING.

Using the quantities defined in Figures 1 and 9b, the double scattering ratio is seen to be

$$S_2 = \iint_{V_1 V_2} \left[I(\theta_1)/I(0)\right] \cdot \left[R_o^2/R_1^2 r_{12}^2 R_2^2\right] \cdot \sigma(\theta^1)\sigma(\theta^{11}) n^2 \exp \left[-\sigma n(r_1 + r_{12} + r_2)\right] A(\theta_2) E(E_n) dV_1 dV_2 \qquad (7)$$

An analytical solution of this integral seems quite involved, if not hopeless, for the geometry of the ring scatterer. In order to get some feeling for the manner in which the double scattering varies with the thickness of the ring, we have chosen to calculate the straight through double scattering from a right circular cylinder assuming isotropic scattering ($\sigma(\theta') = \text{constant}$). In order to simplify this case as much as possible, let the neutron beam, incident on the circular end of the cylinder, be parallel to the cylinder axis, and let the detector sensitivities $A(\theta_2) = E(E_n) = 1$. Also let $r_1 + r_2$ be replaced by an approximate mean value d, the thickness of the cylinder. Equation (7) then reduces to

$$S_2 \doteq \left[\sigma^2 n^2/16\pi^2 R_2^2\right] \cdot \exp(-\sigma n d) \iint_{V_1 V_2} r_{12}^{-2} \exp(-\sigma n r_{12}) dV_1 dV_2 \qquad (8)$$

If the exponential function is expanded and the first three terms retained, $S_2$ reduces to the following:

$$S_2 = \left[\sigma^2 n^2 a^4 / 16 R_2^2\right] . \exp(-\sigma n d).(X - \sigma n d Y + \frac{1}{2}\sigma^2 n^2 a^2 \zeta^2) \qquad (9)$$

where

$$X = -2d^2/a^2 . \ln d/a + 2d^2/a^2 \operatorname{Sin} h^{-1} d/2a$$
$$+ \operatorname{Cos} h^{-1}(1 + d^2/2a^2) + 2d^2/a^2 - d^4/4a^4 \qquad (10)$$
$$-(1-d^2/2a^2).\left[(1 + d^2/2a^2)^2 - 1\right]^{1/2}$$

$$Y = 8 \int_0^\infty \left[ xd/2a - \exp(-xd/2a) \operatorname{Sin} h(xd/2a) \right] J_1(x) \operatorname{Sin} x . dx/x^4 \qquad (11)$$

and

$$\zeta^2 = d^2/a^2 \qquad (12)$$

The integration of x was facilitated by the use of a theorem in vector analysis[12]. The integration of Y can be effected by recognising that the integral corresponds to the electrostatic energy of a uniform volume distribution of charge[13].

If the single scattering ratio $S_1$ is calculated for the right circular cylinder under the same assumptions, then the effective single scattering cross section is given by

$$\bar{\sigma}/\bar{\sigma} = 1 + (\sigma na/4)\, G(d/a) \tag{13}$$

where

$$G(d/a) = (a/d)(X - \sigma naY + \tfrac{1}{2}\sigma^2 n^2 a^2 Z) \tag{14}$$

and is written only as a function of d/a since it varies but slowly with $\sigma na$ as may be seen in Figure 4. By considering the mean curve to apply to all cases of interest the function G becomes a function of d/a only.

To apply the calculations of the right circular cylinder to the case of the ring scatterer, we assume that except for multiplying angular functions, the geometrical variation of the single and double scattering ratios is given correctly a after associating the radial thickness of the ring scatterer, b, with the radius of the cylinder, a.

If, instead of isotropic scattering, one takes the other extreme of an angular distribution peaked strongly in the forward direction, one finds that the single scattering-ratio in the ring scattering varies as d exp $(-\sigma nd)$ whereas the double scattering ratio varies as $d^2$ exp $(-\sigma nd)$; thus leading

to a linear variation of the apparent single scattering cross section with the thickness of the ring.

## REFERENCES


1. Kikuchi, Aoki and Wakatuki, Proc. Phys. Math. Soc. Japan 21, 410 (1939); Wakatuki and Kikuchi, Proc. Phys. Math. Soc. Japan 21, 656 (1939); Wakatuki, Proc. Phys. Math. Soc. Japan 22, 430 (1940).

2. Amaldi, Bocciarelli, Cacciapuoti, and Trabacchi, International Conference on Fundamental Particles and Low Temperature, Vol, 1, The Physical Society, London (1947).

3. Remund and Ricamo, Helv. Phys. Acta. 25, 441 (1952).

4. Walt and Barschall, Phys. Rev. 90, 714 (1953).

5. Feshback, Porter and Weisskopf, Phys. Rev. 90, 166 (1953).

6. H. H. Barschall, Phys. Rev. 86, 431 (1952); Miller, Adair, Bockelman, and Darden, Phys. Rev. 88, 83 (1952).

7. Feshback, Porter and Weisskopf, Bull. Amer. Phys. Soc. 28, No. 3, 29 (1953).

8. W. F. Hornyak, Rev. Sci. Instru. 23, 264 (1952).

9. The authors are indebted to Dr. Hornyak for supplying them with a Lucite-zinc sulphide molded button.

9. Hunter and Richards, Phys. Rev. 76, 1445 (1949).

10. Neresen and Darden, Phys. Rev. 89, 775 (1953).

11. Nuclear Data, Natl. Bureau of Standards Circular 499 (1950).

12. H. B. Phillips, Vector Analysis (John Wiley and Sons, Inc., New York, 1933). See Chapter III.

13. W. R. Smythe, Static and Dynamic Electricity (McGraw-Hill Book Co., Inc., New York, 1939). See Chapter V.

14. Final Report of the Fast Neutron Data Project, NYO-636.